



Article

Coordinated Sliding Mode and Model Predictive Control for Enhanced Fault Ride-Through in DFIG Wind Turbines

Ahmed Muthanna Nori ¹, Ali Kadhim Abdulabbas ¹  and Tawfiq M. Aljohani ^{2,*} 

¹ Electrical Engineering Department, College of Engineering, University of Basrah, Basrah 61001, Iraq; eng.ahmed.m@uobasrah.edu.iq (A.M.N.); ali.abdulabbas@uobasrah.edu.iq (A.K.A.)

² Department of Electrical Engineering, College of Engineering at Yanbu, Taibah University, Yanbu Al-Bahr 41911, Saudi Arabia

* Correspondence: torwi@taibahu.edu.sa

Abstract

This work proposes an effective control technique for enhancing the stability of Doubly Fed Induction Generator-Based Wind Turbines (DFIG-WTs) connected to the grid during voltage sag and swell events, ensuring the reliable and efficient operation of wind energy systems integrated with the grid. The proposed approach integrates a Dynamic Voltage Restorer (DVR) in series with a Wind Turbine Generator (WTG) output terminal to enhance the Fault Ride-Through (FRT) capability during grid disturbances. To develop a flexible control strategy for both unbalanced and balanced fault conditions, a combination of feedforward and feedback control based on a sliding mode control (SMC) for DVR converters is used. This hybrid strategy allows for precise voltage regulation, enabling the series compensator to inject the required voltage into the grid, thereby ensuring constant generator terminal voltages even during faults. The SMC enhances the system's robustness by providing fast, reliable regulation of the injected voltage, effectively mitigating the impact of grid disturbances. To further enhance system performance, Model Predictive Control (MPC) is implemented for the Rotor-Side Converter (RSC) within the back-to-back converter (BTBC) configuration. The main advantages of the predictive control method include eliminating the need for linear controllers, coordinate transformations, or modulators for the converter. Additionally, it ensures the stable operation of the generator even under severe operating conditions, enhancing system robustness and dynamic response. To validate the proposed control strategy, a comprehensive simulation is conducted using a 2 MW DFIG-WT connected to a 120 kV grid. The simulation results demonstrate that the proposed control approach successfully limits overcurrent in the RSC, maintains electromagnetic torque and DC-link voltage within their rated values, and dynamically regulates reactive power to mitigate voltage sags and swells. This allows the WTG to continue operating at its nominal capacity, fully complying with the strict requirements of modern grid codes and ensuring reliable grid integration.

Keywords: doubly fed induction generator; feedforward-feedback; dynamic voltage restorer; fault Ride-Through; voltage sags; voltage swells; predictive control; slide mode control



Academic Editors: Abdelali El Aroudi, Elhoussin Elbouchikhi and Abdelmajid Abouloifa

Received: 23 May 2025

Revised: 17 July 2025

Accepted: 24 July 2025

Published: 28 July 2025

Citation: Nori, A.M.; Abdulabbas, A.K.; Aljohani, T.M. Coordinated Sliding Mode and Model Predictive Control for Enhanced Fault Ride-Through in DFIG Wind Turbines. *Energies* **2025**, *18*, 4017. <https://doi.org/10.3390/en18154017>

Copyright: © 2025 by the authors.

Licensee MDPI, Basel, Switzerland.

This article is an open access article distributed under the terms and conditions of the Creative Commons Attribution (CC BY) license (<https://creativecommons.org/licenses/by/4.0/>).

1. Introduction

A. Background and Literature Review

Over the past few decades, the global energy landscape has undergone a significant transformation, driven by the desire to replace fossil fuels and their escalating environ-

mental and economic costs. In response to these challenges, renewable energy sources have become a crucial solution for mitigating the upcoming power crisis and meeting the growing need for renewable power. Among the various renewable energy technologies, wind power has gained prominence due to its abundance, environmental friendliness, and rapid growth worldwide [1].

The growing integration of wind energy into modern power systems has highlighted the urgent need for advanced control and protection technologies to maintain grid stability and reliability. Various countries have adopted distinct strategies to expand their wind generation capabilities [2]. In regions with mature wind energy sectors, grid codes have been developed to address the specific challenges associated with wind power integration. A critical requirement for successful integration is the Fault Ride-Through (FRT) capability of Wind Turbine Generators (WTGs), which ensures that they can remain operational during grid disturbances. Grid codes typically mandate both High-Voltage Ride-Through (HVRT) and Low-Voltage Ride-Through (LVRT) performance to enable WTGs to support the grid during voltage fluctuations [3]. As illustrated in Figure 1a, WTGs should stay linked to the grid as long as the terminal voltage remains within a defined gray-shaded region. If the voltage deviates beyond this range, disconnection is permitted without compromising system integrity. Furthermore, when terminal voltages lie within the 0.9 to 1.1 per unit (p.u.) range, WTGs are expected to continue operation, although brief disconnections may be necessary under certain voltage excursions outside this band [4].

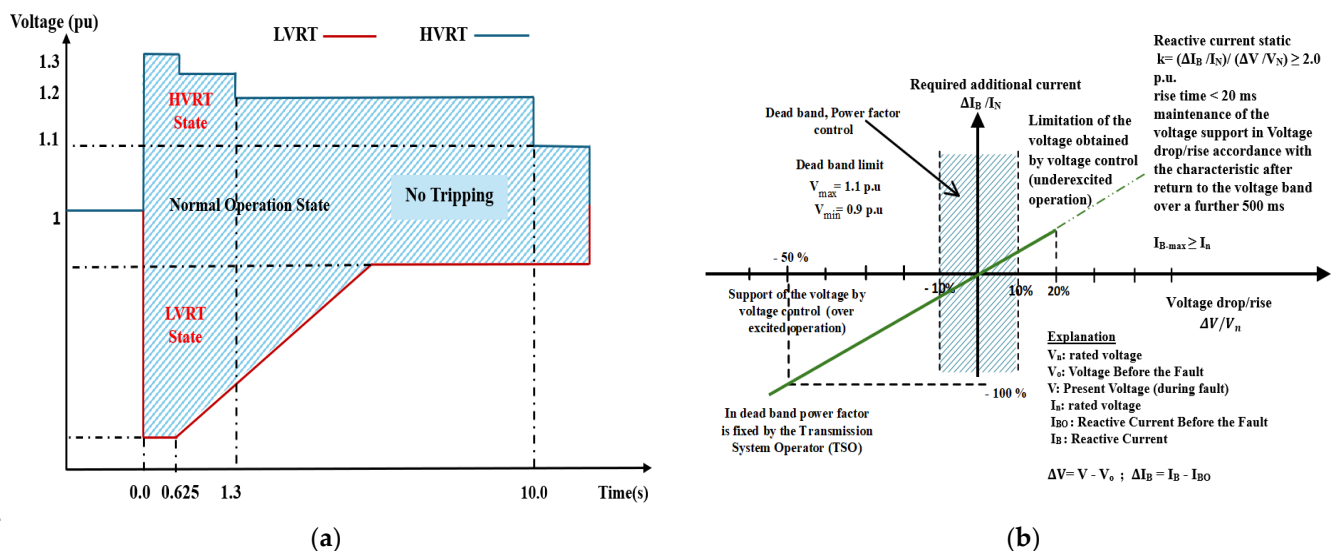


Figure 1. The grid code requirements: (a) an example of FRT grid codes [4]; (b) demanded voltage support during onshore wind plant disturbances—German code [5].

Additionally, the wind turbines (WTs) must provide voltage support to the grid during faults by generating reactive power. For every 1% increase in the amplitude of the voltage drop, a reactive current injection of no more than 2% of the rated current should be supplied to compensate. This voltage regulation must be activated within 20 milliseconds of the fault's onset. After the voltage fault is cleared, within 500 milliseconds, the voltage support should return to a dead band of $\pm 10\%$. Figure 1b shows the reactive current output from the WT, which is used to regulate the voltage when it exceeds the specified tolerance range of $\pm 10\%$ from the nominal power level [5].

The most prevalent wind power generator is the variable-speed wound-rotor doubly fed induction generator (DFIG) [6,7]. It is an induction machine featuring a wound rotor; the stationary windings are directly integrated with the electrical grid, whereas the rotating windings are coupled to the utility network through a bidirectional back-to-back converter

(BTBC). This converter supports the grid by controlling both the Rotor-Side Converter (RSC) and the Grid-Side Converter (GSC). The RSC is used to capture the maximum wind power available and regulate the active and reactive power supplied. The GSC is connected to the grid through a grid filter and is utilized to regulate the DC bus voltage, as well as to manage the bidirectional flow of real and reactive components between the rotor of DFIG and the utility grid [7].

Despite its advantages, the DFIG is very susceptible to grid voltage sags and swells. The RSC and the DC-link capacitor may sustain damage due to these disturbances, which can cause overcurrent in the RSC and excessive voltage across the capacitor [8]. To mitigate the adverse effects of faults on the DFIG, various solutions have been developed, which can be broadly classified into two categories: software-based and hardware-based approaches. The first category involves altering the converters' control methods in the event of a malfunction [9]. However, this approach is typically effective only for small voltage fluctuations and cannot meet stringent grid code requirements on its own [10]. The second category includes hardware solutions that involve protective devices designed to limit the increase in rotor current and DC voltage. These devices include crowbar circuits, series R-L circuits, Series Braking Resistors (SBRs), Braking Choppers (BCs), Superconducting Fault Current Limiters (SFCLs), and Series Dynamic Braking Resistors (SDBRs). Additionally, reactive power devices (RPDs) and energy storage devices (ESDs) are also considered in this category. RPDs improve the DFIG's performance by injecting reactive power, with examples including the Static Synchronous Compensator (STATCOM), Shunt Voltage Compensator (SVR), Unified Power Quality Conditioner (UPQC), and Dynamic Voltage Restorer (DVR). ESDs rely on storing active power during faults, using devices like supercapacitors, batteries, compressed air energy storage, and flywheels [11,12]. Different types of FRT techniques are illustrated in Figure 2.

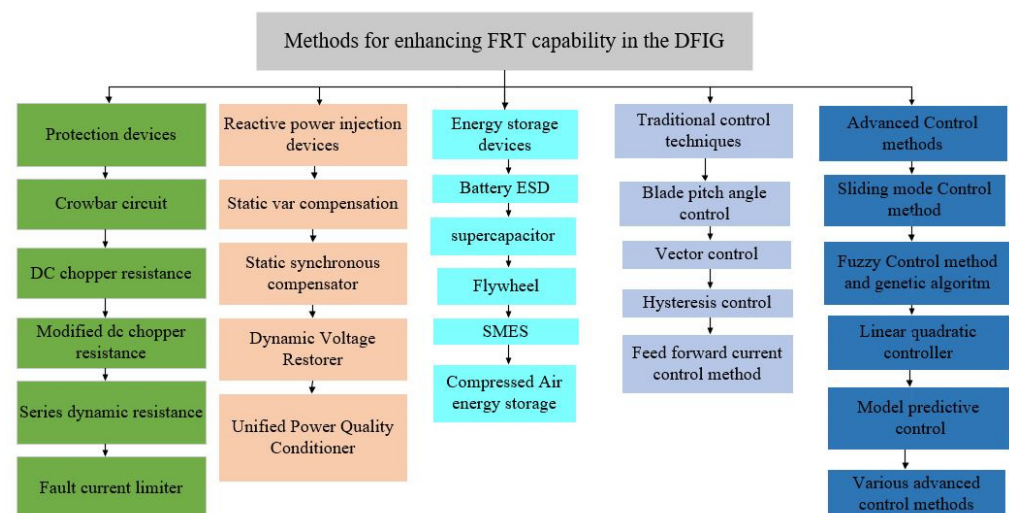


Figure 2. Types of hardware-based FRT solutions for DFIG systems [12].

Crowbars are frequently utilized to prevent overcurrent conditions in the generator's windings, as well as to stabilize the DC-link voltage [13]. To manage surplus energy and maintain the DC-link voltage at a safe level, a BC is installed in parallel with the DC bus [14]. Additionally, an SFCL placed in series with the rotor has been explored as a protective solution to mitigate rotor overcurrent in grid-connected DFIG systems [15]. Reference [16] proposes embedding a crowbar protection circuit within the DFIG's DC-link to improve its LVRT performance, utilizing a hybrid storage system composed of SMES and battery technologies. To mitigate power fluctuations in wind turbines, a lithium-ion battery storage unit is integrated into the DFIG's DC-link through the use of a bidirectional DC-DC

converter, thereby improving grid stability and power reliability [17]. While protective devices are essential for safety and energy storage devices provide temporary power balancing, neither directly stabilizes grid voltage nor ensures compliance with grid codes under severe fault conditions.

To ensure the continuous operation of a grid-connected DFIG-based wind turbine (DFIG-WT) during voltage drops at the point of common coupling (PCC), flexible AC transmission system (FACTS) technologies have been suggested as an effective alternative. These devices are typically employed either independently or in coordination with the control mechanisms of RSC and GSC to regulate voltage stability at the PCC. Essentially, FACTS devices contribute to reactive power compensation in response to voltage sag conditions, and their effectiveness relies on the implementation of a well-designed control algorithm. In [18], the application of SVRs and STATCOMs has demonstrated effectiveness in enhancing voltage stability by delivering the necessary Swift reactive power injection. Meanwhile, ref. [19] discusses the development of the two-stage wind turbine-based DR for voltage control and social welfare purposes. Furthermore, ref. [20] shows that the DVR can improve the FRT capability of DFIG systems by injecting the appropriate compensating voltage at the turbine terminals. Among the various FACTS technologies, the DVR emerges as the most efficient solution for improving the performance of DFIG-WT systems. It is particularly effective in restoring voltage levels at the turbine terminals by mitigating voltage sags, swells, and harmonic distortions. Unlike the STATCOM, which often necessitates the use of a crowbar circuit to safeguard the RSC from excessive current, the DVR allows the wind turbine to stay connected to the grid and continue operation throughout voltage disturbances—without requiring additional protective components. Additionally, the DVR offers advantages in terms of its compact size and lower cost compared to the STATCOM [21].

B. Motivation and Objective of Study

Most existing studies primarily focus on voltage sags, with limited investigation into voltage swells and severe fault conditions. Reference [22] studied the enhancement of LVRT capabilities in Type-3 WTs using a DVR and an active disturbance rejection control (ADRC) scheme. The study shows improved LVRT performance and reactive power support, even during severe voltage drops. In reference [23], the authors improved LVRT performance in DFIG-based wind energy systems using PI controllers and a series grid-side converter (SGSC). Simulations showed a 77.6% improvement in rotor current compared to PI control and 20.61% compared to PI + DIFCL. Reference [24] proved that the DVR can compensate for both voltage sags and swells during different types of fault scenarios, but severe fault scenarios have not been thoroughly explored. This gap emphasizes the importance of conducting a comprehensive analysis of the transient performance of DFIG-WT systems and improving the stability and FRT capability of DFIG-WTs during voltage sags, swells, and severe disturbances. These grid issues can disrupt turbine performance, making advanced control strategies essential for efficient operation. To address this, a robust control strategy is needed for the converters of WTG and DVR to mitigate disturbances, ensuring that parameters, including terminal voltage, rotor and output currents, active and reactive power, and DC voltage, remain within acceptable limits during faults. This allows the WTG to operate at nominal capacity, optimizing performance and ensuring compliance with grid requirements. These are the major motivations and objectives of our work.

C. Contributions of This Study

In order to mitigate grid issues, this study presents an effective control strategy that combines a DVR with an enhanced BTBC control scheme, aimed at improving the FRT capability of WTG. The key contributions of this study are as follows:

1. **Advanced Control Approach:** The DVR utilizes a combined feedforward and feedback (CFFFB) control scheme with voltage control based on SMC. This allows for dynamic adjustment of the injected voltage to compensate for both voltage sags and swells, ensuring fast and precise voltage restoration even during severe fault conditions.
2. **Integration of Predictive Control:** The BTBC control scheme integrates predictive control into the RSC, enabling the prediction and regulation of rotor currents and electromagnetic torque to ensure that they remain within permissible limits. This predictive capability facilitates rapid dynamic adjustments and significantly enhances system performance during disturbances.
3. **Dynamic Behavior Analysis:** This study investigates the dynamic behavior of key system variables (e.g., stator voltage and current, rotor current, DC-link voltage, electromagnetic torque, rotor speed, and active/reactive power) under both balanced and unbalanced voltage sag and swell conditions, with and without the proposed protection strategy.
4. **Effective Suppression of Disturbances:** The proposed protection scheme effectively suppresses variations in terminal voltage, rotor current, electromagnetic torque, and active/reactive power output during disturbances. It also maintains the DC-link voltage within its rated range throughout these events.
5. **Reactive Power Support:** The system dynamically supplies or absorbs reactive power to mitigate voltage disturbances, ensuring compliance with modern grid codes and maintaining stable wind turbine operation, even under severe fault conditions.
6. **Superior Performance in Comparison to Previous Works:** A comparison with prior studies demonstrates that the proposed scheme significantly improves LVRT capabilities for grid-integrated DFIGs.

The structure of this paper is organized as follows: Section 2 provides an in-depth analysis of the DFIG-WT system under fault conditions. Section 3 introduces the modeling approach for the DFIG-WT system coupled with a DVR. The control strategies for this integrated system are discussed in Section 4. Section 5 presents the simulation results for a 2 MW DFIG system using MATLAB/Simulink 2024a under various grid fault scenarios. Finally, Section 6 concludes this paper.

2. Performance of WTG During Fault

In a power system, a fault refers to an abnormal event that results in a disturbance or complete outage of the electrical supply. Symptoms of such faults include unbalanced phases, undervoltage, and overcurrent, which indicate a malfunction within the system. A detailed theoretical study of the transient dynamics of the DFIG under fault conditions is provided in this paper. It also examines the link between grid voltages and rotor currents. The equations governing the voltage and flux in the DFIG can be represented as follows [25]:

$$\vec{v}_s = R_s \vec{i}_s + \frac{d\vec{\psi}_s}{dt} \quad (1)$$

$$\vec{v}_r = R_r \vec{i}_r + \frac{d\vec{\psi}_r}{dt} \quad (2)$$

$$\vec{\psi}_s = L_s \vec{i}_s + L_m \vec{i}_r \quad (3)$$

$$\vec{\psi}_r = L_r \vec{i}_r + L_m \vec{i}_s \quad (4)$$

The expressions for stator and rotor inductances are provided as follows:

$$L_s = L_m + L_{ls} \quad (5)$$

$$L_r = L_m + L_{lr} \quad (6)$$

where \vec{v}_s and \vec{i}_s represent the stator voltage and current, respectively; \vec{v}_r and \vec{i}_r are the rotor voltage and current, respectively; L_s and R_s denote the stator inductance and resistance, respectively; L_r and R_r denote the rotor inductance and resistance, respectively; $\vec{\psi}_s$ and $\vec{\psi}_r$ represent the stator and rotor flux space vectors, respectively. L_m represents the magnetizing inductance, while L_{lr} is the leakage inductance of the rotor. L_{ls} is the leakage inductance of the stator.

The rotor flux is almost the same as the stator flux produced by the grid when the stator is directly linked to it. However, a slight difference may occur between the two fluxes, primarily due to leakage inductances. From Equations (3) and (4), the relationship between both fluxes is given by the following:

$$\vec{\psi}_r = \frac{L_m}{L_s} \vec{\psi}_s + \sigma L_r \vec{i}_r \quad (7)$$

where $\sigma = 1 - L_m^2 / L_s L_r$ is the leakage coefficient.

By combining Equations (7) and (2), the following expression for the rotor voltage is obtained:

$$\vec{v}_r = \frac{L_m}{L_s} \frac{d\vec{\psi}_s}{dt} + \left(R_r + \sigma L_r \frac{d}{dt} \right) \vec{i}_r \quad (8)$$

Therefore, the rotor voltage can be separated into two components. The first component represents the electromotive force (EMF) induced by the stator flux within the rotor, which corresponds to the voltage at the rotor's open-circuit terminals, where $\vec{i}_r = 0$. The equation for this induced EMF is given by

$$\vec{v}_{or} = \frac{L_m}{L_s} \frac{d\vec{\psi}_s}{dt} \quad (9)$$

The second component appears only when current flows through the rotor. It arises from the voltage drop across the rotor's transient inductance, σL_r , and the rotor resistance R_r . The rotor voltage \vec{v}_r can be expressed in Equation (10) as a function of the stator flux and rotor current, as shown below [23]:

$$\vec{v}_r = \vec{v}_{or} + R_r \vec{i}_r + \sigma L_r \frac{d\vec{i}_r}{dt} \quad (10)$$

From Equation (10), the equivalent circuit of the DFIG, viewed from the rotor's perspective, is illustrated in Figure 3. Under normal operating conditions, the output voltage of the RSC must be sufficiently high to overcome the induced EMF, enabling it to regulate the rotor currents and satisfy the generator's torque demands. A transient EMF is generated in the rotor windings due to a grid disturbance, which consists of both homogeneous and non-homogeneous components. To mitigate the non-homogeneous EMF and control rotor current, the RSC must adjust the output voltage after the homogeneous component decays exponentially. During unbalanced faults, the RSC also manages both the positive and negative sequence components of rotor current to ensure stable and reliable operation of the generator. The following subsections focus on two types of grid voltage disturbances: voltage sag and voltage swell.

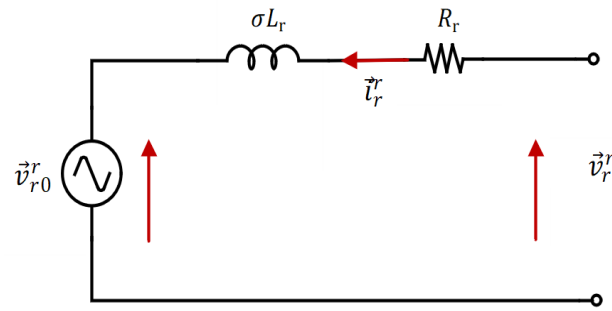


Figure 3. Equivalent circuit of the rotor.

2.1. Transient Behavior Analysis of DFIG During a Voltage Sag Event

Single Line-to-Ground (SLG) faults are the most common and destructive of asymmetrical faults in wind-power systems. One of the three lines in such a condition fails while the other two remain intact. The analysis considers that the DFIG operates under normal conditions prior to the time of occurrence of the asymmetrical fault, represented by time t_0 . Equation (11) describes the voltage of the stator during such a fault [23]:

$$\begin{aligned}\vec{v}_s &= \vec{v}_{s+} + \vec{v}_{s-} \\ \vec{v}_{s+} &= \begin{cases} V_{s+} e^{j\omega_s t}, & t_0 < 0 \\ (1-p)V_{s+} e^{j(\omega_s t + \theta_1)}, & t_0 \geq 0 \end{cases} \\ \vec{v}_{s-} &= \begin{cases} 0, & t_0 < 0 \\ qV_{s-} e^{-j(\omega_s t + \theta_2)}, & t_0 \geq 0 \end{cases}\end{aligned}\quad (11)$$

where the variables with subscript (+) and (−) represent the positive and negative sequence components, respectively. p and q denote the drops in the negative and positive sequence voltage components, respectively; θ_1 and θ_2 are the phase angle shifts of the sequence voltage, and ω_s denotes synchronous speed.

By disregarding the stator resistance, the constant stator flux, which is induced by the stator voltage, can be determined as follows [26]:

$$\begin{aligned}\vec{\psi}_s &= \vec{\psi}_{s+} + \vec{\psi}_{s-} \\ \vec{\psi}_{s+} &= \begin{cases} \frac{V_{s+}}{j\omega_s} e^{j\omega_s t}, & t_0 < 0 \\ \frac{(1-p)V_{s+}}{j\omega_s} e^{j(\omega_s t + \theta_1)}, & t_0 \geq 0 \end{cases} \\ \vec{\psi}_{s-} &= \begin{cases} 0, & t_0 < 0 \\ \frac{qV_{s-}}{-j\omega_s} e^{-j(\omega_s t + \theta_2)}, & t_0 \geq 0 \end{cases}\end{aligned}\quad (12)$$

The stator flux dynamic response can be evaluated using Equations (11) and (12) with an error margin ranging from 10% to 20% [26].

$$\vec{\psi}_s = \frac{(1-p)V_{s+}}{j\omega_s} e^{j(\omega_s t + \theta_1)} + \frac{qV_{s-}}{-j\omega_s} e^{-j(\omega_s t + \theta_2)} + \vec{\psi}_{sn} e^{-\frac{t}{\tau_s}} \quad (13)$$

where $\vec{\psi}_{sn} = 1 - \frac{(1-p)V_{s+} e^{j\theta_1}}{j\omega_s} + \frac{qV_{s-}}{j\omega_s} e^{-j\theta_2}$ and $\tau_s = \frac{\sigma L_s}{R_s}$ represent the initial value of the natural stator flux and the time constant of the stator, respectively.

As shown in Equation (13), for $t \geq t_0$, the stator flux consists of non-homogeneous components, which are transient fluxes that prevent discontinuities in the magnetic state of the machine when the operating point changes and that decay exponentially, and homogeneous (or natural) components. The homogeneous component remains steady.

By substituting the natural flux from Equation (13) into Equation (9), the rotor EMF can be determined:

$$\begin{aligned} \vec{v}_{or}^r = & k_s s(1-p)V_{s+}e^{j(s\omega_s t + \theta_1)} + k_s(2-s)qV_{s-}e^{-j((2-s)(\omega_s t + \theta_2))} \\ & - k_s\left(\frac{1}{\tau_s} + j\omega\right)\vec{\psi}_{sn}^r e^{-(\frac{1}{\tau_s} + j\omega)t} \end{aligned} \quad (14)$$

where $s = (\omega_s - \omega)/\omega_s$ is the slip of the DFIG, ω is the rotor angular speed, and $k_s = \frac{L_m}{L_s}$ is the coupling factor.

The induced EMF has three portions, as given in Equation (14). The first component depends on the slip s and depth of the positive sequence voltage sag p . The second component involves $(2-s)$ and negative sequence voltage q , which can become very high when the DFIG operates at super-synchronous speeds. Positive and negative sequence voltages have frequencies of $s\omega_s$ and $(2-s)\omega_s$, respectively. With its dominant frequency is ω , the latter component can be damped exponentially. It should be noted that the initial values of the three parts can be influenced by the phase shift following grid faults.

On the other hand, a severe symmetrical three-phase fault with low impedance causes the stator flux and voltage to drop to zero almost instantaneously. However, based on the flux decay theorem, the stator flux decays more slowly than the voltage due to the machine's electromagnetic inertia. This slower decay is characterized by the stator time constant, which introduces an inertial time lag in the system, $\tau_s = \frac{L_s}{R_s}$, impacting the EMF, \vec{v}_{r0}^r . The stator flux undergoes exponential decay during a symmetrical fault and can be represented as follows [27]:

$$\vec{\psi}_{sf} = \vec{\psi}_s e^{-t/\tau_s} \quad (15)$$

The voltage induced in the rotor within a stationary reference frame is expressed as

$$\vec{v}_{or}^s = \frac{L_m}{L_s} \left(\frac{d}{dt} - j\omega \right) \vec{\psi}_s \quad (16)$$

Taking the time derivative of Equation (15) and substituting into Equation (16) gives

$$\vec{v}_{or}^s = -k_s \left(\frac{1}{\tau_s} + j\omega \right) \vec{\psi}_s e^{-t/\tau_s} \quad (17)$$

The above equation is expressed in the rotor reference frame, with the assumption to neglect $\frac{1}{\tau_s}$:

$$\vec{v}_{or}^r = -k_s(j\omega) \vec{\psi}_s e^{-j\omega t} \quad (18)$$

The pre-fault stator flux, $\vec{\psi}_s = \frac{\vec{v}_s}{j\omega_s} e^{-j\omega_s t}$, can be substituted into Equation (18) to derive Equation (19).

$$\vec{v}_{or}^r = -k_s(1-s)V_s \quad (19)$$

Since k_s and V_s are constants, the rotor-induced voltage magnitude, $|\vec{v}_{or}^r|$, is directly proportional to $(1-s)$.

2.2. Transient Behavior Analysis of DFIG During a Voltage Swell Event

It is assumed that at $t = t_0$, the grid voltage suddenly swells symmetrically from V_s to $(1+p)V_s$. Accordingly, the grid voltage can be formulated as [28]

$$\vec{v}_s = \begin{cases} V_s e^{j\omega_s t} & \text{for } t < t_0 \\ (1+p)V_s e^{j\omega_s t} & \text{for } t \geq t_0 \end{cases} \quad (20)$$

The stator flux consists of two components: the steady-state flux $\vec{\psi}_s$, defined before and after a voltage swell, as shown in Equation (21), and the natural flux $\vec{\psi}_{sn}$, which maintains continuity in the stator flux when the flux magnitude changes proportionally with the stator voltage. This component of flux appears only during the transient condition of sag or swells and is given as in Equation (22). As evident from Equation (22), the transient flux dies out with the stator time constant τ_s , and it has an exponentially diminishing negative dc value and is proportional to the ratio of swell. If the height of the swell is larger, the initial magnitude of natural flux will increase proportionally. The magnitude of the steady state flux after swell is proportional to the stator voltage after swell [29].

$$\vec{\psi}_s = \begin{cases} \frac{V_s}{j\omega_s} e^{j\omega_s t} & \text{for } t < t_0 \\ \frac{(1+p)V_s}{j\omega_s} e^{j\omega_s t} & \text{for } t \geq t_0 \end{cases} \quad (21)$$

$$\vec{\psi}_{sn} = \frac{-pV_s}{j\omega_s} e^{-(t-t_0)/\tau_s} e^{j\omega_s t_0} \quad (22)$$

The stator voltage swell has influence on the rotor voltage of DFIG. The rotor voltage also comprises steady state and natural components and is the effective sum of these two. The rotor voltage natural component vector \vec{v}_{rn} is given by Equation (23). It is evident from Equation (23) that \vec{v}_{rn} is proportional to $(1-s)$ and height of rise.

The operating range of slip for the DFIG is relatively small, which results in a higher value for the natural component. If the swell height is small, the value of \vec{v}_{rn} will have minimal impact on the RSC. However, if the swell height is significantly larger, it could potentially damage the RSC of the DFIG. The steady-state rotor voltage after a swell, denoted as \vec{v}_{rf} , is directly proportional to both the magnitude of the DFIG stator voltage and the slip, as expressed in Equation (24). The total rotor voltage with RSC connected to the rotor will be the sum of the steady state and natural components, as shown in Equation (25).

$$\vec{v}_{rn}^r = k_s(pV_s)(1-s)e^{-\frac{t}{\tau_s}} e^{-j\omega t} \quad (23)$$

$$\vec{v}_{rf}^r = k_s(1+p)V_s e^{js\omega_s t} \quad (24)$$

$$\vec{v}_r^r = \vec{v}_{rn}^r + \vec{v}_{rf}^r + \vec{t}_r R_r + \sigma L_r \frac{d\vec{i}_r^r}{dt} \quad (25)$$

where \vec{v}_{rn} is the natural (transient) rotor voltage caused by the swell.

The additional term accounts for the rotor resistance and leakage inductance effects. When the grid voltage suddenly swells, the rotor-induced voltage in the rotor reference frame can be expressed as [30]

$$\vec{v}_{or}^r = \vec{v}_{rn}^r + \vec{v}_{rf}^r \quad (26)$$

From Equation (10), the expression for the rotor phase-a voltage can be written in the rotor reference frame as

$$\vec{v}_{ra}^r = \text{Re}[\vec{v}_{or}^r] + R_r \vec{i}_r^r + \sigma L_r \frac{d\vec{i}_r^r}{dt} \quad (27)$$

The linear differential equation governing the rotor current $i_{ra}(t)$ is given by

$$\frac{d\vec{i}_{ra}^r}{dt} + \frac{R_r}{\sigma L_r} \vec{i}_{ra}^r = \frac{1}{\sigma L_r} \left(\vec{v}_{ra}^r - \text{Re}[\vec{v}_{or}^r] \right) \quad (28)$$

Substituting the voltage expression from Equation (26) into the linear differential Equation (28) yields the following result:

$$\begin{aligned} \vec{i}_{ra}^r = \vec{i}_{ra}^r(t_0^-) &- \frac{1}{\sigma L_r} \frac{\tau_r}{1+\tau_r^2 \omega_{sl}^2} [V_r \cos \beta - V_s k_s s(1+p)] + \frac{1}{\sigma L_r} V_s (1-s) p k_s \frac{\tau_r}{1+\tau_r^2 \omega^2} \left\} e^{-\frac{t}{\tau}} + \frac{V_r}{\sigma L_r} \right. \\ &\cdot \frac{\tau_r}{\sqrt{1+\tau_r^2 \omega^2}} \sin(\omega_{sl} t + \beta + \varphi_1) - \frac{V_s}{\sigma L_r} k_s s(1+p) \frac{\tau_r}{\sqrt{1+\tau_r^2 \omega_{sl}^2}} \sin(\omega_{sl} t + \varphi_2) - \frac{V_s}{\sigma L_r} k_s p(1 \\ &- s) \frac{\tau_r}{\sqrt{1+\tau_r^2 \omega^2}} \sin(\omega t + \varphi_1) \end{aligned} \quad (29)$$

where β is the angle of the phase-a rotor voltage at the instant the fault begins, and ω_{sl} is slip angular frequency ($\omega_{sl} = \omega_s - \omega$): $\tau = \frac{\tau_r \tau_s}{\tau_s - \tau_r}$, $\tau_r = \frac{\sigma L_r}{R_r}$, $\varphi_1 = \tan^{-1}(1/\tau_r \omega)$, and $\varphi_2 = \tan^{-1}(1/\tau_r \omega_{sl})$.

It can be noted from Equation (29) that when p is small, the transient effect is minimal, and the RSC is not significantly stressed. In contrast, when p is large, the peak rotor current increases proportionally, which can potentially damage the RSC.

3. Structure and Modeling of the Proposed System

The structure depicted in Figure 4 consists of a WT with a DFIG and a DVR. The DVR, which is powered by an Energy Storage System (ESS), is connected in series with the WT terminals through an LC filter and an ideal transformer, ensuring voltage compensation during sag or swell events. The DFIG is highly susceptible to voltage fluctuations, as its stator windings are directly linked to the grid. Additionally, the strong coupling between the stator and rotor flux means that voltage imbalances or harmonic distortions can induce severe oscillations in electromagnetic torque, stator and rotor currents, DC-link voltage, and overall output power, potentially compromising the stability of the system. To mitigate these issues, the proposed WECS integrates the WTG with the DVR. The modeling of each component is detailed below.

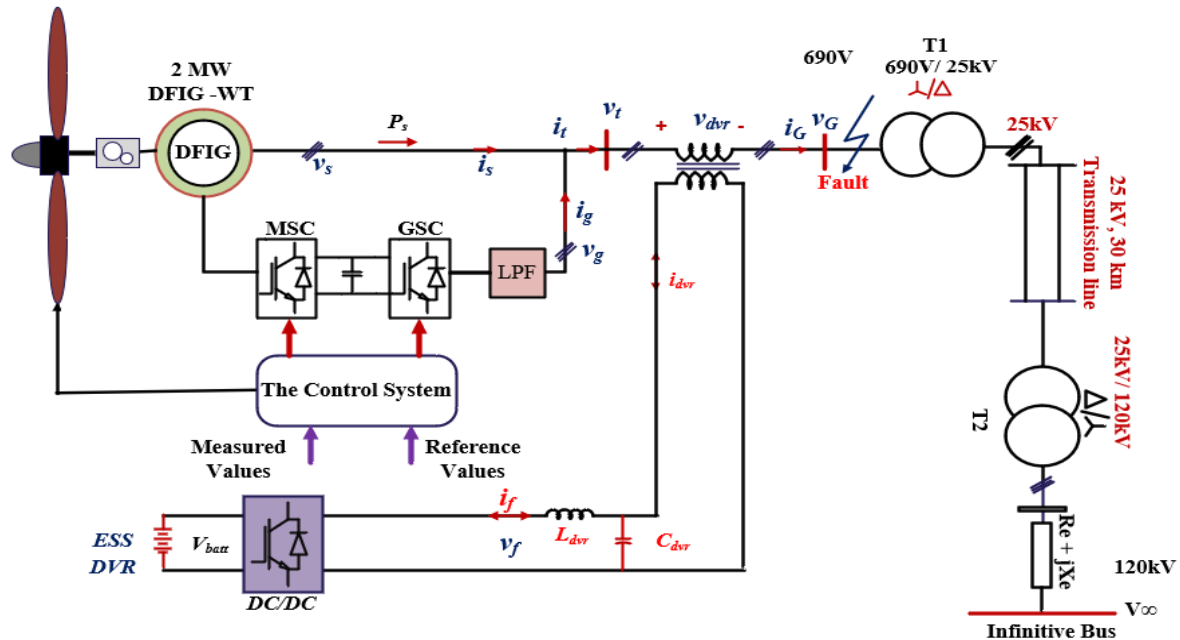


Figure 4. DFIG-based grid-connected understudy system.

3.1. Modeling of BTBC

The power flow through the rotor circuit is influenced by both super- and sub-synchronous operating modes, which requires the power converter controlling the generator's operating point to be bidirectional. The dynamic model in a three-phase (abc)

stationary reference frame is derived using the AC equivalent circuit of the BTBC, as illustrated in Figure 5 [31]:

$$C_g \frac{d}{dt} v_{cg} = i_g - i_1 \quad (30)$$

$$L_g \frac{d}{dt} i_1 = v_{cg} - R_g i_1 - m_1 v_{dc} \quad (31)$$

$$C_{dc} \frac{d}{dt} v_{dc} = m_1 i_1 - m_2 i_2 \quad (32)$$

$$L_r \frac{d}{dt} i_r = m_2 v_{dc} - v_r \quad (33)$$

where i_g represents the grid-side phase current, and i_i denotes the converter-side phase current. v_{dc} and v_{cg} are the voltages of the DC-link and filter capacitor, respectively. C_{dc} is the DC-link capacitance. R_g represents resistance, and L_g represents the inductance of the filter connecting the BTBC to the AC systems. v_r is the rotor voltage, and m_1 and m_2 are the modulating signals constrained by $|m_1, m_2| \leq 1$. Additionally, v_g represents the grid voltage.

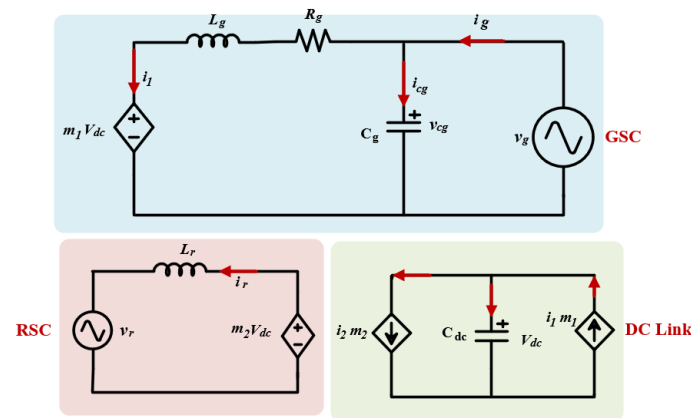


Figure 5. Model state of the BTBC-equivalent circuit. (**Upper**) Circuit for GSC with LC filter, (**lower right**) circuit for DC-link, and (**lower left**) circuit for RSC.

3.2. Modeling of DVR

The DVR is a voltage-source converter (VSC) that generates an AC output voltage continuously and adds it in series with the DFIG's terminal voltage, thereby compensating for voltage sags, swells, or harmonics and restoring the nominal stator voltage. The DVR is designed to handle the full power rating of the wind turbine, as grid codes require complete voltage sag compensation during fault conditions. The power rating of the DVR regulated by the in-phase compensation approach is as follows [32]:

$$S_{dvr} = \sum_{k=a,b,c} \left[V_{dvr,k}^{ref} \cdot I_L \right] \quad (34)$$

where $V_{dvr,k}^{ref}$ represents the RMS voltage supplied by the DVR in phase k , and I_L represents the RMS load current.

In Figure 4, $v_{f,abc}$ represents the three-phase voltage generated by DVR, which depends on the modulation indices m_a , m_b , and m_c :

$$v_{f,abc} = \frac{m_{abc} V_{batt}}{2} \quad (35)$$

Assuming that the DVR is lossless, the active power balance gives

$$i_B = \frac{\sum_{k=a}^c m_k i_{f,k}}{2} \quad (36)$$

Assuming that the injected transformer is ideal, the current/voltage relationships between the primary/secondary can be expressed as follows:

$$\begin{aligned} v_{dvr} &= v_t - v_G \\ i_{dvr} &= -i_g \end{aligned} \quad (37)$$

where v_{dvr} represents the compensation value, and v_t and v_G denote the terminal voltage of the WES and grid voltage, respectively.

The LC filter's mathematical model is formulated as follows [22]:

$$\begin{aligned} v_f &= L_{dvr} \frac{di_f}{dt} + v_{dvr} \\ i_f &= C_{dvr} \frac{dv_c}{dt} + i_{dvr} \end{aligned} \quad (38)$$

where i_f and i_{dvr} denote the DVR-generated current and compensation current, respectively, and L_{dvr} and C_{dvr} are the parameters of the LC filter.

In this study, a DVR based on an in-phase compensation scheme is employed to generate voltage without the need for phase-shifting compensation, as shown in Figure 6. The in-phase compensation approach is particularly effective in ensuring grid stability and improving power quality during voltage disturbances. The active power exchanged between the DVR and the power grid is given by the following expression:

$$\begin{aligned} P_{dvr} &= P_L - P_g = (3 \cdot V_L \cdot I_L \cdot \cos \Psi) - \sum_{k=a,b,c} [V_{g,abc}^{ref} \cdot I_L \cdot \cos \Psi] \\ V_{dvr,abc}^{ref} &= \sqrt{2} |V_L - V_{g,abc}^{ref}| \end{aligned} \quad (39)$$

where δ is the shift in the phase of the grid voltage during a voltage sag, and Ψ is the phase shift between the current and voltage of the load. V_g and V'_g represent the RMS grid voltage before and after the sag, respectively. V_L and V'_L represent the RMS load voltage before and after the sag, respectively. I_L and I'_L represent the RMS load current before and after the sag, respectively, and V_{dvr} is the RMS DVR compensation voltage.

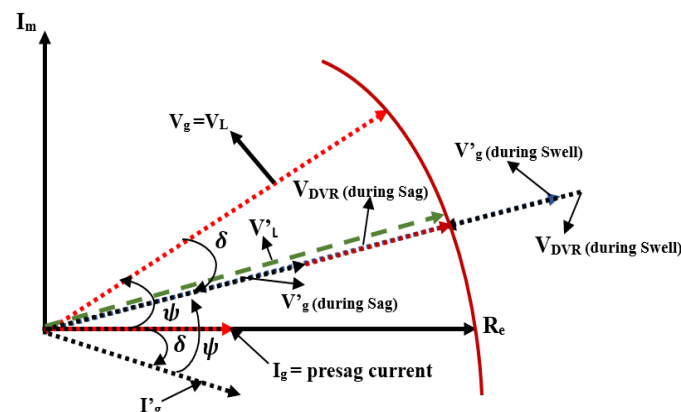


Figure 6. In-phase compensation-based DVR compensation scheme.

4. The Proposed Control Schemes

The proposed control scheme is developed to improve the performance and stability of the DFIG-WT system integrated with a DVR. As illustrated in Figure 4, the system comprises three primary power conversion systems: the RSC, the GSC, and the DVR. Each

of these converters is crucial for maintaining the efficient operation of the DFIG-WT system under both normal and fault conditions. This section presents a detailed analysis of the control strategies employed for each converter, focusing on their individual and collective contributions to the system's overall performance. The control strategies are designed to address the unique challenges posed by grid disturbances, such as voltage sags and swells, while ensuring compliance with modern grid codes. The proposed adaptive control scheme leverages advanced techniques, including predictive control for the RSC, conventional PI control for the GSC, and SMC for the DVR, to achieve robust and efficient operation under varying grid conditions.

4.1. BTBC Control

The BTBC consists of the RSC, the DC-link capacitor, and the GSC. Controlling the reactive power injected by the DFIG, which guarantees operations as per the unity power factor and the achievement of Maximum Power Point Tracking (MPPT), are the main goals of RSC control. On the other hand, regulating the reactive power exchange with the grid, regardless of the direction and magnitude of the rotor power flow, and maintaining a constant DC-link voltage are the main objectives of the GSC control.

MPC for RSC

The suggested control technique for the RSC, illustrated in Figure 7, integrates MPC for the robust and precise regulation of rotor currents. The reference electromagnetic torque (T_{em}^*), obtained from the MPPT algorithm, is utilized to produce i_{rq}^* . From the reference reactive power of the stator (Q_s^*), i_{rd}^* can be obtained. The reactive power is set to zero ($Q_s^* = 0$). These two reference currents are subsequently fed into the MPC algorithm to determine the dq -axis reference voltages, v_{rq}^* and v_{rd}^* , which can be expressed as [33]

$$i_{rq}^* = -\frac{2 L_s T_{em}^*}{3 n_p L_m |\vec{\psi}_s|}, i_{rd}^* = \frac{|\vec{\psi}_s|}{L_m} - \frac{2 L_s}{3 L_m \omega_s |\vec{\psi}_s|} \cdot Q_s^* \quad (40)$$

where n_p is number of pole pairs.

The state-space representation of the dynamic equations governing the direct and quadrature components can be expressed by reformulating these equations into a system of first-order differential equations:

$$\begin{aligned} \frac{dx}{dt} &= Ax + Bu + w \\ y &= Cx \end{aligned} \quad (41)$$

where:

$$\begin{aligned} x &= \begin{bmatrix} i_{rd} \\ i_{rq} \end{bmatrix}, u = \begin{bmatrix} v_{rd} \\ v_{rq} \end{bmatrix}, w = \begin{bmatrix} 0 \\ -\frac{\omega_{sl} L_m}{\sigma L_s L_r} |\vec{\psi}_s| \end{bmatrix} \\ A &= \begin{bmatrix} -\frac{R_r}{\sigma L_r} & \omega_{sl} \\ -\omega_{sl} & -\frac{R_r}{\sigma L_r} \end{bmatrix}, B = \begin{bmatrix} \frac{1}{\sigma L_r} & 0 \\ 0 & \frac{1}{\sigma L_r} \end{bmatrix}, C = \begin{bmatrix} 1 & 0 \\ 0 & 1 \end{bmatrix} \end{aligned}$$

The zero-order hold (ZOH) approach is used to transform the continuous system into its discrete form as follows:

$$\begin{aligned} x(k+1) &= A_d x(k) + B_d u(k) + G_d w(k) \\ y(k) &= C_d x(k) \end{aligned} \quad (42)$$

where

$$A_d \approx I + A_c T = \begin{bmatrix} 1 - \frac{TR_r}{\sigma L_r} & \omega_{sl} T \\ -\omega_{sl} T & 1 - \frac{TR_r}{\sigma L_r} \end{bmatrix}, B_d \approx BT = \begin{bmatrix} \frac{T}{\sigma L_r} & 0 \\ 0 & \frac{T}{\sigma L_r} \end{bmatrix}, G_d = \begin{bmatrix} T & 0 \\ 0 & T \end{bmatrix}, C_d = C$$

where T represents the sampling period.

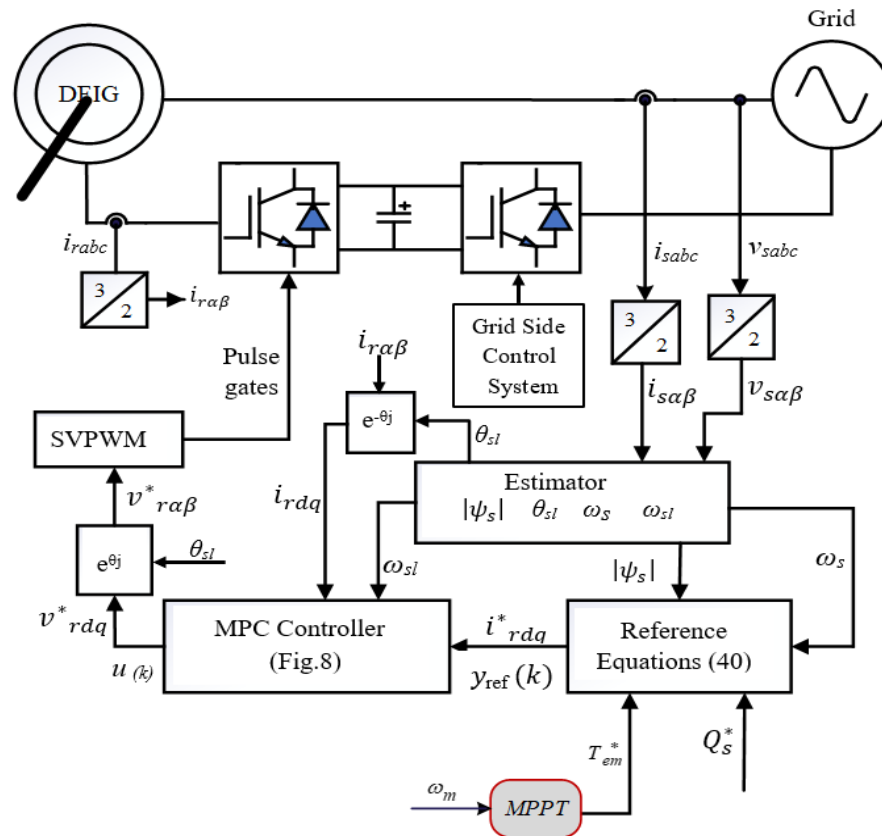


Figure 7. DFIG control diagram.

The prediction of future outputs can be achieved by advancing and iterating Equation (42). Finally, by iteratively applying and reformulating this process, all predicted outputs are represented in a concise matrix form, as shown below [34]:

$$\mathcal{Y} = \mathcal{A}\mathcal{y} + \mathcal{B}\mathcal{U} + \mathcal{G}\mathcal{W} \quad (43)$$

where

$$\mathcal{A} = \begin{bmatrix} C_d A_d & C_d A_d^2 & \dots & C_d A_d^{N_y} \end{bmatrix}^T, \quad \mathcal{B} = \begin{bmatrix} C_d B_d & 0 & \dots & 0 \\ C_d A_d B_d & C_d B_d & \ddots & 0 \\ \vdots & \vdots & \ddots & \vdots \\ C_d A_d^{N_y-1} G_d & C_d A_d^{N_y-2} G_d & \dots & C_d G_d \end{bmatrix}, \quad \mathcal{G} = \begin{bmatrix} C_d G_d & 0 & \dots & 0 \\ C_d A_d G_d & C_d G_d & \dots & 0 \\ \vdots & \vdots & \ddots & \vdots \\ C_d A_d^{N_y-1} G_d & C_d A_d^{N_y-2} G_d & \dots & C_d G_d \end{bmatrix}.$$

The predicted disturbances, control signals, and outputs are defined as follows:

$$\mathcal{W} = \begin{bmatrix} w(k) & w(k+1) & \dots & w(k+N_y) \end{bmatrix}^T, \quad \mathcal{U} = \begin{bmatrix} u(k) & u(k+1) & \dots & u(k+N_u) \end{bmatrix}^T, \quad (44)$$

$$\mathcal{Y} = \begin{bmatrix} y(k+1) & y(k+2) & \dots & y(k+N_y) \end{bmatrix}^T$$

In Equation (44), N_y represents the control horizon, which corresponds to the controller output predictions, while N_u represents the prediction horizon, referring to the number of samples and system output predictions ahead.

Cost functions are usually convex functions of predicted errors and control efforts. The matrix cost function is

$$J = (\mathcal{Y}_{\text{ref}} - \mathcal{Y})^T \mathcal{W}_y (\mathcal{Y}_{\text{ref}} - \mathcal{Y}) + \mathcal{U}^T \mathcal{W}_u \mathcal{U} \quad (45)$$

The elements on the primary diagonal of the weighting matrix correspond to the error and control action, respectively, as outlined below:

$$\mathcal{W}_y = \begin{bmatrix} W_y & \dots & 0 \\ \vdots & \ddots & \vdots \\ 0 & \dots & W_y \end{bmatrix} \in \mathbb{R}^{2N_y \times 2N_y}, \quad \mathcal{W}_u = \begin{bmatrix} W_u & \dots & 0 \\ \vdots & \ddots & \vdots \\ 0 & \vdots & W_u \end{bmatrix} \in \mathbb{R}^{2N_u \times 2N_u} \quad (46)$$

Furthermore, the weighting matrices \mathcal{W}_y and \mathcal{W}_u are defined as $\mathcal{W}_y = \begin{bmatrix} W_{y,d} & W_{y,12} \\ W_{y,12} & W_{y,q} \end{bmatrix}$ and $\mathcal{W}_u = \begin{bmatrix} W_{u,d} & W_{u,12} \\ W_{u,12} & W_{u,q} \end{bmatrix}$, respectively, where $W_{y,d}$, $W_{y,12}$, $W_{y,q}$, $W_{u,d}$, $W_{u,12}$, and $W_{u,q}$ are constants. The set of future references is represented by Equation (47):

$$\mathcal{Y}_{\text{ref}} = \begin{bmatrix} y_{\text{ref}}(k+1) & \dots & y_{\text{ref}}(k+N_y) \end{bmatrix}^T \quad (47)$$

The optimal control signal sequence is found by minimizing Equation (45) with respect to \mathcal{U} , which involves solving $\nabla_{\mathcal{U}} J = 0$ and isolating \mathcal{U} , yielding

$$\mathcal{U} = \left(\mathcal{B}^T \mathcal{W}_y \mathcal{B} + \mathcal{W}_u \right)^{-1} (\mathcal{Y}_{\text{ref}} - \mathcal{A}y - \mathcal{G}\mathcal{W}). \quad (48)$$

In practice, the first two elements of the control law in Equation (48), i.e., $u(k) = \mathcal{U}_{(1-2)}$, are employed, as only the control signal for the next iteration is used. Figure 7 illustrates the RSC control diagram, which includes the other control elements [35].

The current references, $y_{\text{ref}}(k)$, are calculated using Equation (40). The measured currents, $i_{r,abc}$, are transformed into the stator's synchronous frame of reference using the Park and Clarke transforms. MPC controllers employ these data with flux $|\vec{\psi}_s|$ and slip velocity ω_{sl} to compute the control law, as shown in Figure 8.

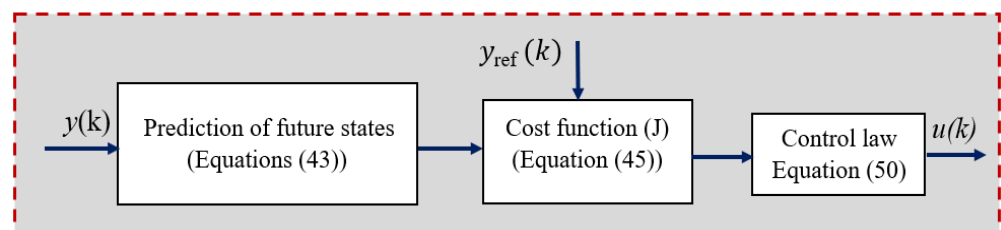


Figure 8. MPC controller.

The result is then converted into the rotor frame reference, v_{rdq} , and applied using space vector pulse-width modulation.

Since only the control signal for the current time is applied to the system, Equation (48) simplifies to Equation (49).

$$\Delta \mathcal{U} = \mathcal{K}(\mathcal{Y}_{\text{ref}} - \mathcal{A}y - \mathcal{G}\mathcal{W}). \quad (49)$$

Here, the gain matrix \mathcal{K} is defined as

$$\mathcal{K} = \begin{bmatrix} 1 & \dots & 0 \end{bmatrix} \left(\mathcal{B}^T \mathcal{W}_y \mathcal{B} + \mathcal{W}_u \right)^{-1}$$

Sequentially, the control law is expressed as

$$\Delta u = \mathcal{K}(\mathcal{Y}_{\text{ref}} - \mathcal{A}y - \mathcal{G}\mathcal{W}). \quad (50)$$

The closed-loop diagram of MPC, shown in Figure 9, illustrates the control action.

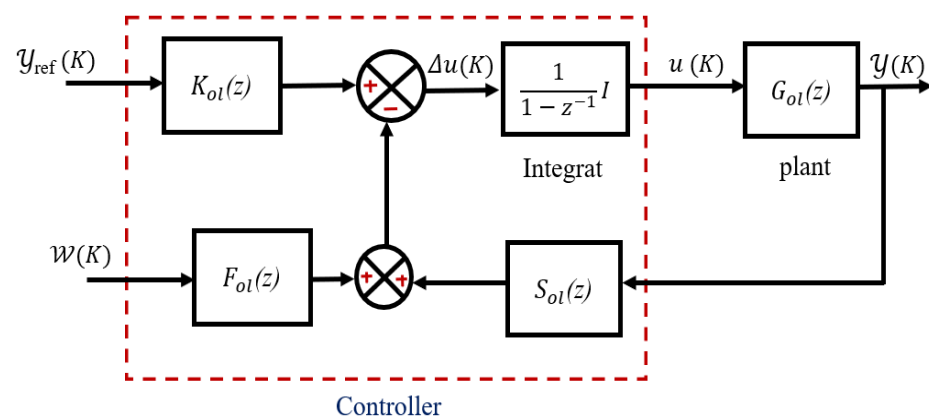


Figure 9. Close loop diagram of MPC [35].

The plant transfer matrix, ignoring the disturbance, is given by

$$G_{ol} = (zI - A_d)B_d^{-1} \quad (51)$$

The closed-loop transfer matrix, as illustrated in Figure 9, is expressed in Equation (52):

$$G_{cl} = K_{ol}(z)I_{ol}(z)G_{ol}(z)(I + I_{ol}(z)G_{ol}(z)S_{ol}(z))^{-1} \quad (52)$$

where $I_{ol}(z) = \frac{1}{1-z^{-1}}I$ represents an integrator.

4.2. SMC of the DVR

The DVR control scheme is a critical component of the studied system designed to detect, mitigate, and compensate for voltage disturbances in the DFIG-WT. The suggested control algorithm incorporates the CFFFB control strategy, which ensures fast and precise voltage restoration under both temporary and permanent fault conditions. The DVR control system begins by detecting the onset of a voltage sag or swell using a dual monitoring approach that combines feedforward and feedback control mechanisms. The feedforward control monitors the grid pre-sag voltage. The feedback control monitors the voltage mitigation on the DFIG side after DVR. This dual monitoring ensures accurate detection of voltage disturbances and enables rapid response to faults. Figure 10 shows the DVR control approach.

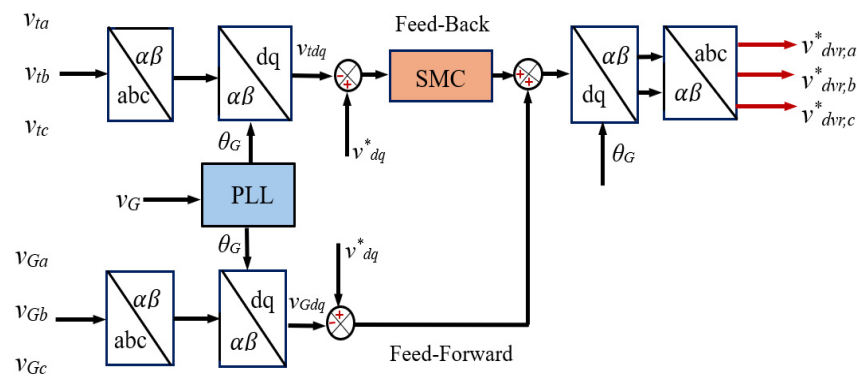


Figure 10. The control scheme of DVR with SMC.

The grid voltage v_G is fed into a PLL block, which extracts the grid phase angle to generate the sine and cosine signals required for the abc/dq transformation. The DFIG terminal voltage v_t is also measured and transformed into v_{td} and v_{tq} . These components are compared with the reference voltages v_{dq}^* . The e_{dq} in Equation (54) is then fed to the input of the SMC [36]:

$$\begin{aligned} e_d &= v_d^* - v_{td} \\ e_q &= v_q^* - v_{tq} \end{aligned} \quad (53)$$

The SMC utilizes a fast-switching regulator to guide the system's state trajectory towards a specific surface in the state space, known as the sliding surface (SS). The objective is to ensure that the system stays within two essential steps. First, the SS must be defined in a manner that constrains the system's variables to it. The second step involves selecting a feedback controller that drives the system's state toward this SS. The sliding surface plays a central role in the performance of the SMC. In this study, we will denote the SS by the symbol s , and it is defined as follows:

$$s = \dot{e} + ce \quad (54)$$

where c is a constant and positive. The SMC can be implemented using various schemes, ranging from first-order to higher-order approaches. In this study, the super-twisting method will be chosen due to its outstanding performance [37]. The control law for the super-twisting method will be expressed as follows.

$$u = c\sqrt{|s|}\text{sign}(s) + b \int \text{sign}(s)dt \quad (55)$$

The selection of appropriate values for the parameters c and b is crucial for the controller's effectiveness, as their determination significantly influences both the controller's performance and the selection of the SS.

The stability of the Super-Twisting Algorithm (STA-SMC) is analyzed using a Lyapunov function $V(s) = \frac{1}{2}s^2$, which is positive definite and equals zero when $s = 0$, indicating that the system converges to the sliding surface. The time derivative of the Lyapunov function, $\dot{V}(s) = s\dot{s}$, depends on the dynamics of the sliding surface, where $\dot{s} = \ddot{e} + c\dot{e}$ represents the error dynamics of the system. Substituting the SAT-SMC law, $u = c|s|\text{sign}(s) + b \int \text{sign}(s)dt$, into the error dynamics influences the term \ddot{e} , which in turn affects the derivative of the Lyapunov function. For the system to be stable, it is necessary that $\dot{V}(s) < 0$. The combination of the sliding mode control term and the integral term ensures that s converges to zero, thereby making $\dot{V}(s)$ negative and definite. In stable conditions, $\dot{V}(s) < 0$, implying that $\dot{s} < 0$ for $s > 0$ and $\dot{s} > 0$ for $s < 0$, which results in the switching nature of the control law around $s = 0$. This analysis demonstrates that the

SAT-SMC law is effective in stabilizing the system by driving the sliding surface to zero, thereby ensuring system stability.

5. Simulation Results and Discussion

5.1. Simulation Setup

The performance of the DFIG-WT system, coupled with a DVR, is evaluated through simulations and modeling carried out in the MATLAB/Simulink 2024a environment, as shown in Figure 11. The system comprises a 2 MW WTG connected to a 25 kV distribution system through a three-phase 0.69/25 kV transformer rated at 4 MVA. The DVR is integrated into the system to mitigate voltage sags and swells, ensuring stable operation under grid disturbances. An adapted utility grid consists of a 30 km transmission line at 25 kV, which connects the DFIG-WT with the DVR system and a 0.69/25 kV transformer to a 120 KV, 50 Hz variable voltage source through a 25/120 kV transformer.

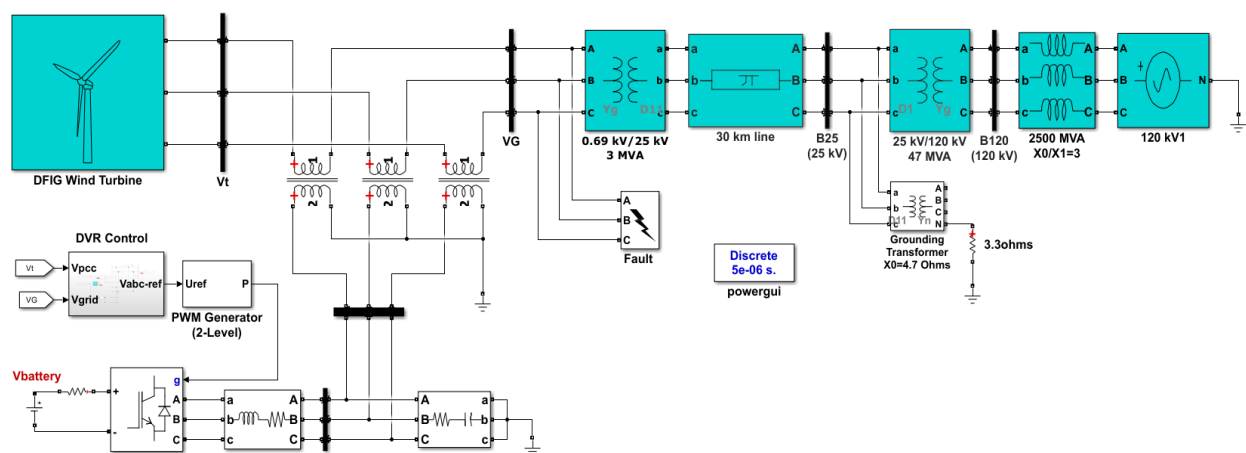


Figure 11. Simulink model of a DFIG -WT with DVR.

5.2. Results and Discussion

The simulation is conducted with a fixed wind speed of 12 m/s to isolate the impact of grid faults on the system's performance. This ensures that any observed fluctuations are only attributable to fault occurrences and the efficacy of the suggested control schemes, which include CFFFB control with voltage regulation based on an SMC for the DVR and MPC for the RSC. The specifications of the DFIG-WT system with the DVR are provided in Table A1. To assess the system's performance in FRT requirements, two fault scenarios are simulated: voltage symmetrical and asymmetric swell/sag faults during the operation of the utility grid, as described below.

5.2.1. Operation of the Proposed System with Different Voltage Sag Conditions

The performance of the proposed system with a DVR is further evaluated under single-phase-to-ground (SLG) and three-phase-to-ground (3LG) faults with a 100% depth. As shown in Figure 12a, without DVR protection, the DFIG terminal voltage undergoes significant distortion during SLG and 3LG faults. The SLG fault leads to asymmetry, while the 3LG fault results in near-complete voltage collapse. In contrast, with DVR protection, the terminal voltage remains stable and symmetrical throughout the disturbance period. This clearly demonstrates the DVR's ability to effectively mitigate voltage sags and preserve terminal voltage integrity. Figure 12b illustrates the DVR's dynamic compensation behavior. The DVR remains inactive under normal conditions and activates promptly during faults. It injects appropriate compensating voltage immediately upon SLG (at 2.5 s) and 3LG (at 3.8 s) faults, thereby restoring the system's voltage. The injected waveform is

proportional and precisely phased, minimizing power quality degradation and ensuring fast fault recovery. As shown in Figure 12c, without DVR, the DC-link voltage experiences surges and oscillations during both fault events, which can strain the converter and risk component failure. In contrast, the DFIG-WT with DVR shows a perfectly stable DC-link voltage, confirming that the DVR not only regulates grid-side voltage but also contributes to internal energy balance and converter protection. The rotor currents (i_{rd} , i_{rq}) and the stator currents (i_{sd} , i_{sq}) depicted in Figure 12d,e surge sharply under fault conditions without DVR, especially during the 3LG event. These unregulated currents could damage the converter or lead to system trips. With DVR enabled, these currents remain controlled and within safe operational limits, demonstrating the controller's robust current regulation and disturbance rejection capability. Figure 12f shows that without DVR, active and reactive power become highly unstable during faults, particularly reactive power, which swings drastically and disturbs power quality. With DVR, both power components remain steady and consistent, enabling the DFIG to continue injecting rated active power and maintaining near-zero reactive power as per grid code requirements. As presented in Figure 12g, torque undergoes large oscillations without DVR, with extreme deviations indicating significant mechanical stress during faults. These oscillations persist even after fault clearance. With DVR protection, the torque remains almost constant and disturbance-free, reducing mechanical fatigue and extending the turbine's operational life. The rotor speed behavior in Figure 12h further highlights the difference. Without DVR, rotor speed fluctuates and recovers slowly after faults, while with DVR, the speed remains smooth and stabilizes quickly, ensuring better system performance.

5.2.2. Operation of the Proposed System with Different Voltage Swell Conditions

As shown in Figure 13, the performance of the proposed DFIG-based wind turbine system, integrated with a DVR, is thoroughly evaluated under both balanced and unbalanced voltage swell conditions. Voltage swell events, defined as temporary increases in grid voltage above nominal levels, can severely impact the stability and power quality of wind energy systems. The DVR's control strategy is specifically designed to mitigate these effects by dynamically injecting compensating voltages. As illustrated in Figure 13a, without DVR protection, the DFIG terminal voltage becomes severely distorted during both the 50% unbalanced swell (2.5 s to 2.6 s) and the 100% balanced swell (3.8 s to 3.9 s), with peak values reaching ± 2000 V, far beyond the rated ± 690 V, indicating a clear inability to suppress transient over voltages. Harmonic distortions persist even after the swell duration, reflecting poor voltage recovery and deteriorated power quality. In contrast, with DVR support, the terminal voltage remains nearly sinusoidal and well-regulated within the rated ± 690 V during these swell events. The DVR voltage compensation is shown in Figure 13b. As shown in Figure 13c, the DVR also significantly stabilizes the DC-link voltage. Without the DVR, the DC-link voltage spikes to over 5500 V, which is nearly five times its nominal value of 1150 V, presenting a risk to DC capacitors and other sensitive components. With the DVR active, the voltage is clamped effectively around 1150 V, confirming superior energy management. Furthermore, Figure 13d,e illustrates that the rotor current components (i_{rd} , i_{rq}) and current components (i_{sd} , i_{sq}) exhibit extreme oscillations without the DVR, reaching magnitudes above 10,000 A, accompanied by severe waveform distortion imposing high stress on the RSC. With DVR compensation, these currents remain balanced and confined within rated limits. The power profile shown in Figure 13f further confirms the DVR's effectiveness. In the absence of DVR, active power fluctuates up to ± 20 MW, and reactive power swings around ± 10 MVAR, undermining grid stability and code compliance. With DVR enabled, active power stabilizes at around 2 MW, while reactive power remains near zero, supporting uninterrupted and regulated power delivery. Mechanical performance is

also improved, as shown in Figure 13g. Without a DVR, electromagnetic torque oscillates violently, reaching $-150,000$ N·m, which may lead to mechanical wear on the turbine shaft and gearbox. With DVR support, torque remains steady at its rated value, avoiding such stresses. Finally, Figure 13h demonstrates that rotor speed fluctuates without DVR due to torque disturbances, while DVR operation maintains it tightly around rated value, ensuring smooth and stable turbine operation throughout voltage swell events.

The findings show that the proposed technique improves the FRT capability of the DFIG, reducing the impact of grid disturbances. The system maintains balanced three-phase values and power quality during faults. The simulation results demonstrate the effectiveness of CFFFB control for the DVR in compensating voltage sags and swells, ensuring continuous operation and protecting the wind turbine from transient conditions. This enhances system reliability, extends the lifespan of rotor and stator windings and sensitive converters, reduces mechanical stress, minimizes harmonic distortions, and improves energy extraction. Thanks to the advanced control strategies, including SMC and MPC, performance is optimized, components are protected, and the operational lifetime of the system is extended, ensuring more reliable and efficient power generation from the DFIG-WT system.

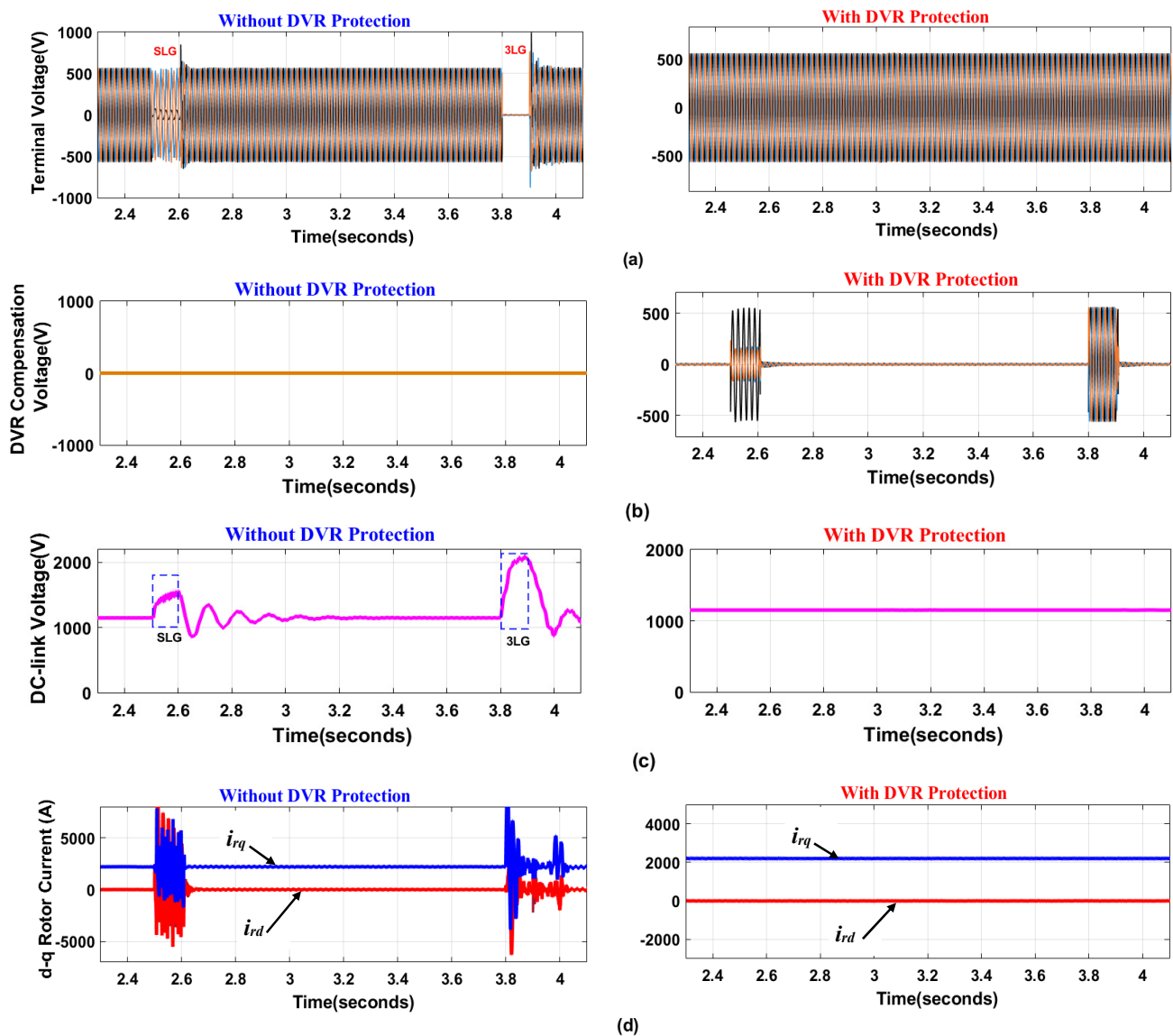


Figure 12. Cont.

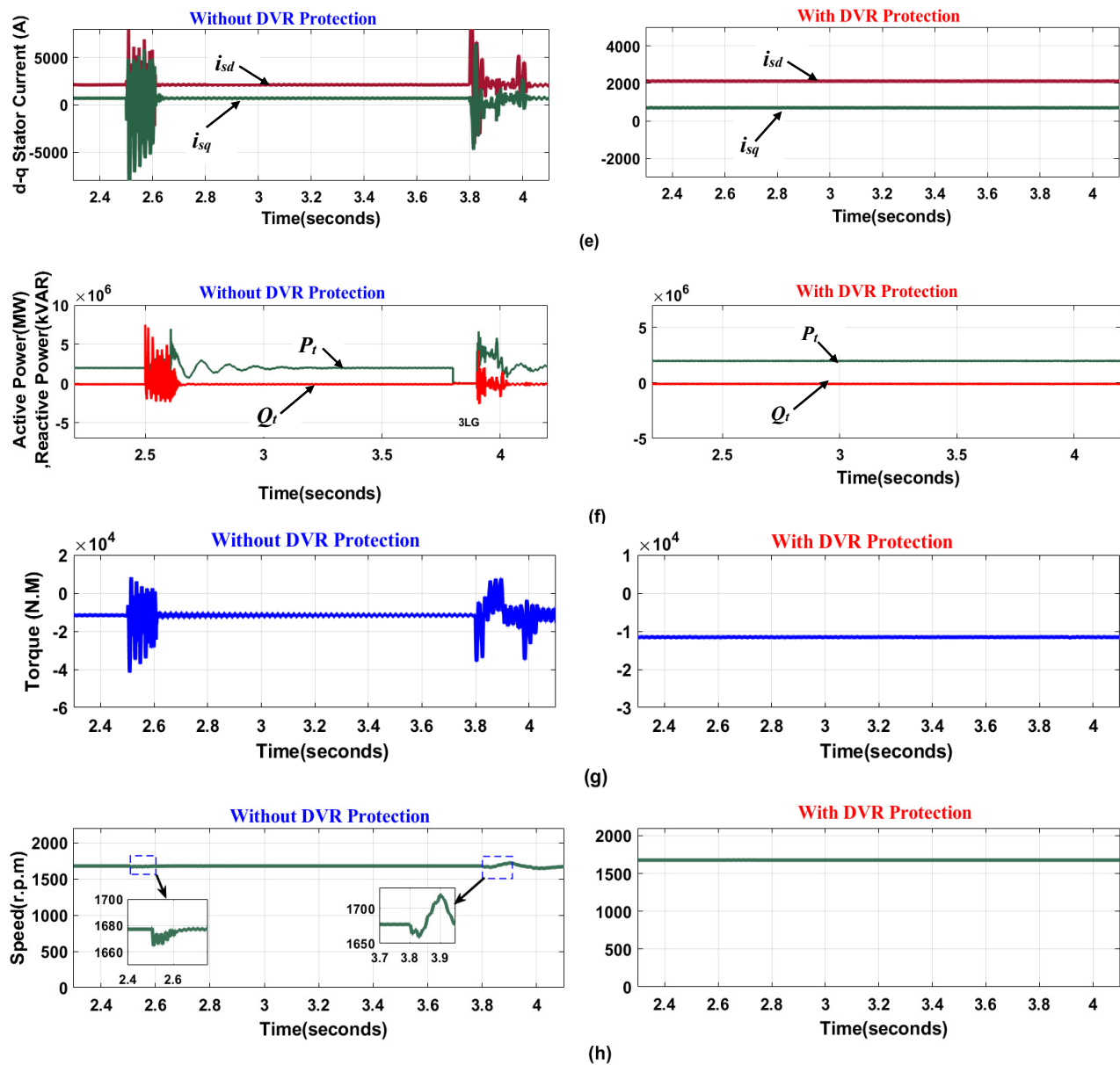


Figure 12. Behavior of WTG under balanced/unbalanced voltage sag conditions with and without DVR. (a) DFIG terminal voltage (V); (b) DVR compensation voltage (p.u); (c) DC-link voltage (V); (d) dq-axis rotor currents (A); (e) dq-axis stator currents; (f) active power (MW) and reactive power (MVar); (g) electromagnetic torque (N.M); (h) rotor speed (r.p.m).

5.3. Comparison with Previous Works

After thoroughly analyzing the performance of the proposed protection scheme, a comprehensive comparison was conducted with previous work [22] to clearly highlight the advantages of the proposed system. This comparison was based on several key performance parameters, including voltage stability, rotor and stator current behavior, DC-link voltage, electromagnetic torque, reactive power handling, and transient response time. The results of the comparison are presented in Table 1.

The findings indicate that the proposed system, which integrates SMC-based DVR protection and employs MPC for the RSC, outperforms the previous work in terms of system stability and response time. Notably, the proposed system exhibits no overshoot in rotor current, stator current, or torque and demonstrates significantly faster transient

recovery. In contrast, the previous work experiences substantial overshoot in both electrical and mechanical quantities of the WTG during fault conditions, as shown in Table A1.

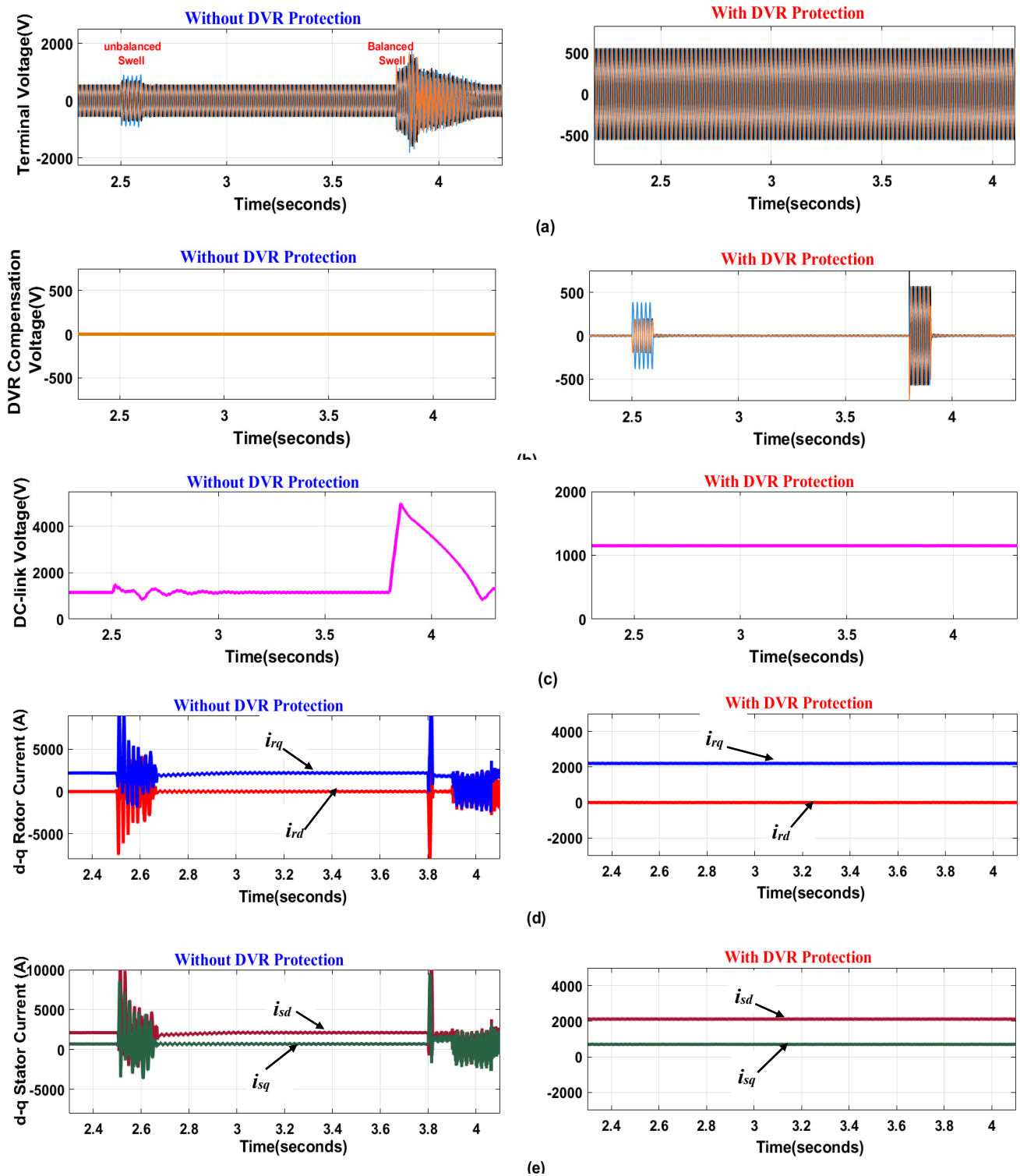


Figure 13. Cont.

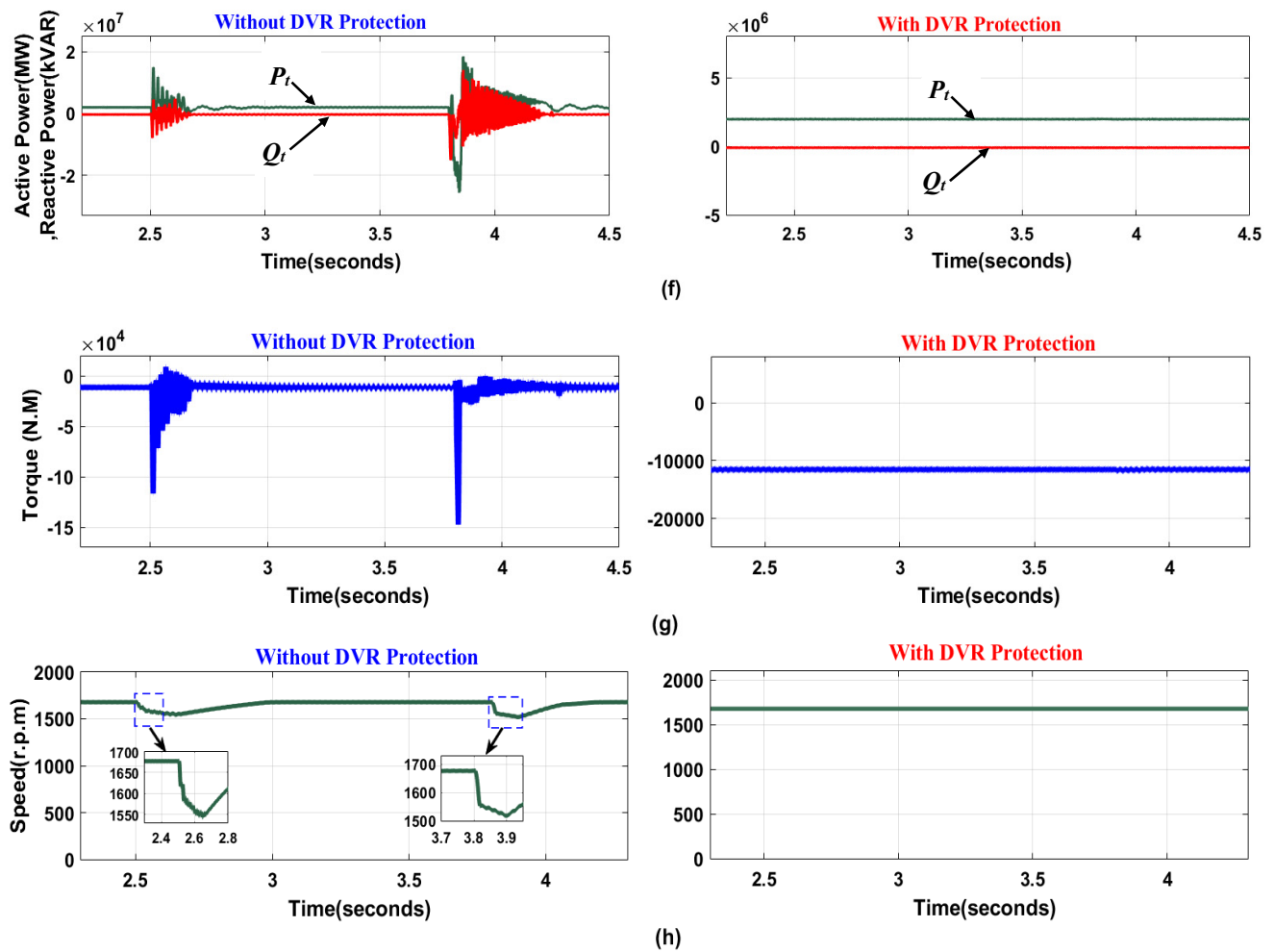


Figure 13. Behavior of WTG under balanced/unbalanced voltage swell conditions with and without DVR. (a) DFIG terminal voltage (V); (b) DVR compensation voltage (p.u); (c) DC-link voltage (V); (d) dq-axis rotor currents (A); (e) dq-axis stator currents; (f) active power (MW) and reactive power (MVar); (g) electromagnetic torque (N.M); (h) rotor speed (r.p.m).

Table 1. Main overshoot parameters of DFIG-WT.

Parameter	Proposed System	Previous Work [22]
Voltage Drop (pu)	100%	95%
Rotor Current (pu)	No overshoot	1.4 (steady state: 0.6)
Stator Current (pu)	No overshoot	1.25 (steady state: 0.6)
DC-Link Voltage (pu)	No overshoot	3.09 (steady state: 3)
Electromagnetic Torque (pu)	No overshoot	1.25 (steady state: 0.6)
Active Power Supplied (pu)	No overshoot	1.04 (steady state: 0.5)
Reactive Power Supplied (pu)	No overshoot	0.3 (steady state: 0.0)

Also, the suggested system in [23] demonstrated improvements in overshoot and oscillations of electromagnetic torque, reaching 1.24 pu, maintaining the rotor current at 0.35 pu, limiting the active power to 5.54 MW, and resulting in a lower reactive power of -9.87 MVar during a three-phase fault. However, it is still compared with the proposed system, which exhibits no overshoot. This comparison clearly highlights the superior

performance and efficiency of the proposed system, ensuring enhanced stability and faster recovery times under fault conditions.

6. Conclusions

This study presents an effective control strategy that integrates a DVR. Specifically, SMC is employed for the DVR, while predictive control is applied to the RSC. This integrated approach ensures robust and stable operation of the WTG under both balanced/unbalanced grid disturbances. The DVR, controlled by the CFFFB control scheme, is crucial to maintain the stator terminal voltage at its nominal level during grid disturbances. The feedforward control provides an immediate response to voltage fluctuations, while the feedback control refines the compensation to eliminate steady-state errors. This dual mechanism ensures precise voltage restoration, even under severe fault conditions. The SMC for the DVR demonstrates exceptional robustness in regulating stator voltages, effectively mitigating overcurrent and preventing damage to the power electronics. Meanwhile, the predictive control for the RSC maintains the rotor current within its specified limits, ensuring stability during transient grid disturbances. Extensive simulations under various fault scenarios, including single-phase and three-phase faults, as well as voltage swells, verify the effectiveness of the proposed control approach. The system maintains stable power exchange with the grid, adhering to unity power factor operations and meeting stringent grid code demands. Additionally, the mechanical stability of the DFIG rotor is preserved, with minimal oscillations in rotor speed and electromagnetic torque, thereby reducing mechanical stress and enhancing the longevity of the turbine components. The results of this research highlight the potential of the proposed control strategy for real-world implementation, offering a reliable and cost-effective solution for enhancing the FRT capability of the WTG. By ensuring continuous operation during grid disturbances, the suggested control scheme enhances the reliability and efficiency of wind energy systems and supports the overall stability and resilience of the energy network. Future work will focus on the experimental validation and optimization of the control parameters for broader application in large-scale wind farms, utilizing optimization methods to determine the predictive model's control parameters. This will help enhance the performance of the model and ensure its effectiveness in real-world applications. The integration of optimization techniques, such as genetic algorithms, particle swarm optimization, or gradient-based methods, will be crucial in fine-tuning the control parameters, ensuring better prediction accuracy and efficiency in predictive control models, especially in complex and dynamic wind farm environments.

Author Contributions: Conceptualization, A.M.N., A.K.A. and T.M.A.; Methodology, A.M.N. and T.M.A.; Software, A.M.N.; Validation, A.M.N.; Formal analysis, A.M.N., A.K.A. and T.M.A.; Investigation, A.M.N., A.K.A. and T.M.A.; Resources, A.M.N. and A.K.A.; Data curation, A.M.N.; Writing—original draft, A.M.N.; Writing—review & editing, A.M.N. and T.M.A.; Visualization, A.M.N.; Supervision, A.K.A. and T.M.A.; Project administration, A.M.N. and T.M.A. All authors have read and agreed to the published version of the manuscript.

Funding: This research received no external funding.

Data Availability Statement: The original contributions presented in the study are included in the article, further inquiries can be directed to the corresponding author.

Conflicts of Interest: The authors declare no conflict of interest.

Appendix A. System Parameters

Table A1. The parameters of the studied system.

DFIG Parameters	Value
Rated power	2 MW
Rated voltage	0.69 kV
Rated wind speed	12 m/s
Rated frequency	50 Hz
Stator resistance	$2.6 \times 10^{-3} \Omega$
Rotor resistance	$2.9 \times 10^{-3} \Omega$
Stator leakage inductance	$87 \times 10^{-6} \text{ H}$
Magnetizing inductance	$2.5 \times 10^{-3} \text{ H}$
Turns ratio	0.34
DC-link voltage of DFIG	1.15 kV
DVR Parameters	Value
Rated power	2 MW
DC-link voltage of DVR	1.2 kV
DC-link capacitor	30,000 μF
The 0.69/25 kV Transformer	Value
Rated power	3 MVA
Leakage resistance	0.025/30 pu
Leakage Inductance	0.025 pu
Transformer base frequency	50 Hz
Transformer rating	0.69/25 kV
The 25/120 kV Transformer	Value
Rated power	47 MVA
Leakage resistance	0.0026667 pu
Leakage Inductance	0.08 pu
Transformer base frequency	50 Hz
Transformer rating	25/120 kV

References

- Li, L.; Liang, Y.; Niu, J.; He, J.; Liu, H.; Li, B.; Li, C.; Cao, Y. The Fault ride-through characteristics of a double-fed induction generator using a dynamic voltage restorer with superconducting magnetic energy storage. *Appl. Sci.* **2023**, *13*, 8180. [\[CrossRef\]](#)
- Yadav, V.V.; Saravanan, B. Technical advances and stability analysis in wind-penetrated power generation systems—A review. *Front. Energy Res.* **2022**, *10*, 1091512. [\[CrossRef\]](#)
- El Karkri, Y.; El Markhi, H.; El Moussaou, H.; Lamhamdi, T. LVRT and HVRT control strategies of Doubly-Fed Induction Generator. *J. Electr. Syst.* **2018**, *14*, 1–20.
- Abdelkader, S.M.; Morgan, E.F.; Megahed, T.F.; Rohouma, W.; Abdel-Rahim, O. A model predictive control strategy for enhancing fault ride through in PMSG wind turbines using SMES and improved GSC control. *Front. Energy Res.* **2023**, *11*, 1277954. [\[CrossRef\]](#)
- Elyaalaoui, K.; Ouassaid, M.; Cherkaoui, M. Dispatching and control of active and reactive power for a wind farm considering fault ride-through with a proposed PI reactive power control. *Renew. Energy Focus* **2019**, *28*, 56–65. [\[CrossRef\]](#)
- Shuaibu, M.; Abubakar, A.; Shehu, A. Techniques for ensuring fault ride-through capability of grid connected dfig-based wind turbine systems: A review. *Niger. J. Technol. Dev.* **2021**, *18*, 39–46. [\[CrossRef\]](#)
- Aljohani, T. Intelligent type-2 fuzzy logic controller for hybrid microgrid energy management with different modes of EVs integration. *Energies* **2024**, *17*, 2949. [\[CrossRef\]](#)

8. Safaei, A.; Hosseini, S.H.; Abyaneh, H.A. Enhancing the HVRT and LVRT Capabilities of DFIG-Based Wind Turbine in an Islanded Microgrid. *Eng. Technol. Appl. Sci. Res.* **2017**, *7*, 2118–2123. [\[CrossRef\]](#)
9. Ghosh, S.; Isbeih, Y.J.; Bhattarai, R.; El Moursi, M.S.; El-Saadany, E.F.; Kamalasadan, S. A Dynamic Coordination Control Architecture for Reactive Power Capability Enhancement of the DFIG-Based Wind Power Generation. *IEEE Trans. Power Syst.* **2020**, *35*, 3051–3064. [\[CrossRef\]](#)
10. Alaboudy, A.H.K.; Mahmoud, H.A.; Elbaset, A.A.; Abdelsattar, M. Technical Assessment of the Key LVRT Techniques for Grid-Connected DFIG Wind Turbines. *Arab. J. Sci. Eng.* **2023**, *48*, 15223–15239. [\[CrossRef\]](#)
11. Qin, B.; Li, H.; Zhou, X.; Li, J.; Liu, W. Low-Voltage Ride-through Techniques in DFIG-Based Wind Turbines: A Review. *Appl. Sci.* **2020**, *10*, 2154. [\[CrossRef\]](#)
12. Moheb, A.M.; El-Hay, E.A.; El-Fergany, A.A. Comprehensive review on fault ride-through requirements of renewable hybrid microgrids. *Energies* **2022**, *15*, 6785. [\[CrossRef\]](#)
13. Musarrat, N.; Fekih, A.; Islam, R. An improved fault ride through scheme and control strategy for DFIG-based wind energy systems. *IEEE Trans. Appl. Supercond.* **2021**, *31*, 1–6. [\[CrossRef\]](#)
14. Guo, Z.; Wang, Z. Analysis of the Impact of Crowbar and Chopper Protection on Low Voltage Ride Through of DFIG. In Proceedings of the IEEE 2024 6th Asia Energy and Electrical Engineering Symposium (AEEES), IEEE, Chengdu, China, 28–31 March 2024; pp. 812–821.
15. Naderi, S.B.; Davari, P.; Zhou, D.; Negnevitsky, M.; Blaabjerg, F. A review on fault current limiting devices to enhance the fault ride-through capability of the doubly-fed induction generator based wind turbine. *Appl. Sci.* **2018**, *8*, 2059. [\[CrossRef\]](#)
16. Li, C.; Cao, Y.; Liu, B.; Qiao, F.; Chen, P. A novel low voltage ride-through scheme for DFIG based on the cooperation of hybrid energy storage system and crowbar circuit. *J. Energy Storage* **2023**, *73*, 108879. [\[CrossRef\]](#)
17. Behabtu, H.A.; Vafaeipour, M.; Kebede, A.A.; Berecibar, M.; Van Mierlo, J.; Fante, K.A.; Messagie, M.; Coosemans, T. Smoothing intermittent output power in grid-connected doubly fed induction generator wind turbines with li-ion batteries. *Energies* **2023**, *16*, 7637. [\[CrossRef\]](#)
18. Qi, J.; Zhao, W.; Bian, X. Comparative study of SVC and STATCOM reactive power compensation for prosumer microgrids with DFIG-based wind farm integration. *IEEE Access* **2020**, *8*, 209878–209885. [\[CrossRef\]](#)
19. Singh, V.; Fozdar, M.; Aljohani, T.; Singh, S.; Malik, H. A two-stage wind power integrated demand response framework under constrained transmission network for social welfare maximization. *Appl. Energy* **2025**, *394*, 126109. [\[CrossRef\]](#)
20. Falehi, A.D.; Torkaman, H. Promoted Supercapacitor Control Scheme Based on Robust Fractional-Order Super-Twisting Sliding Mode Control for Dynamic Voltage Restorer to Enhance FRT and PQ Capabilities of DFIG-Based Wind Turbine. *J. Energy Storage* **2021**, *42*, 102983. [\[CrossRef\]](#)
21. Moghassemi, A.; Padmanaban, S. Dynamic voltage restorer (DVR): A comprehensive review of topologies, power converters, control methods, and modified configurations. *Energies* **2020**, *13*, 4152. [\[CrossRef\]](#)
22. Boulaoutaq, E.M.; Aziz, A.; El Magri, A.; Abbou, A.; Ajaamoum, M.; Rachdy, A. Low-voltage ride-through capability improvement of Type-3 wind turbine through active disturbance rejection feedback control-based dynamic voltage restorer. *Clean Energy* **2023**, *7*, 1091–1109. [\[CrossRef\]](#)
23. Soomro, M.; Memon, Z.A.; Baloch, M.H.; Mirjat, N.H.; Kumar, L.; Tran, Q.T.; Zizzo, G. Performance improvement of grid-integrated doubly fed induction generator under asymmetrical and symmetrical faults. *Energies* **2023**, *16*, 3350. [\[CrossRef\]](#)
24. Bouaziz, F.; Masmoudi, A.; Abdelkafi, A.; Krichen, L. Coordinated Control of Smes and Dvr for Improving Fault Ride-through Capability of Dfig-Based Wind Turbine. *Int. J. Renew. Energy Res. (IJRER)* **2022**, *12*, 359–371.
25. Mosayyebi, S.R.; Shahalami, S.H.; Mojallali, H. Fault ride-through capability improvement in a DFIG-based wind turbine using modified ADRC. *Prot. Control Mod. Power Syst.* **2022**, *7*, 1–37. [\[CrossRef\]](#)
26. Geng, H.; Liu, C.; Yang, G. LVRT capability of DFIG-based WECS under asymmetrical grid fault condition. *IEEE Trans. Ind. Electron.* **2012**, *60*, 2495–2509. [\[CrossRef\]](#)
27. Ananth, D.; Kumar, G.N. Fault ride-through enhancement using an enhanced field oriented control technique for converters of grid connected DFIG and STATCOM for different types of faults. *ISA Trans.* **2016**, *62*, 2–18. [\[CrossRef\]](#)
28. Latif, S.; Savier, J.S. Particle Swarm Optimized Phase Shifted DVR (PSDVR) for High Voltage Ride through in DFIG. *J. Emerg. Trends Electr. Eng.* **2021**, *3*, 1–9.
29. Wang, Y.; Wang, H.; Liu, C.; Xie, L.; Ding, L. An improved HVRT control strategy for DFIG. In Proceedings of the 2020 IEEE/IAS Industrial and Commercial Power System Asia (I&CPS Asia), Online, 13–16 July 2020; pp. 133–137.
30. Le, Z.; Xueguang, W.; Longze, K.; Dong, L.; Fangyuan, L.; Mingxiao, H. Control strategy of doubly-fed induction generator during the grid voltage swell. *J. Eng.* **2019**, *2019*, 1807–1811. [\[CrossRef\]](#)
31. Rosas, E.; Cardenas, V.; Alcala, J.; Nunez, C. Active and reactive current decoupled control strategy applied to a single-phase BTB converter. In Proceedings of the IEEE 2009 6th International Conference on Electrical Engineering, Computing Science and Automatic Control (CCE), Toluca, Mexico, 10–13 January 2009; pp. 1–6.

32. AlGhamdi, S.A. Improvement of fault ride-through capability of grid connected wind turbine based on a switched reluctance generator using a dynamic voltage restorer. *Sustainability* **2023**, *15*, 11061. [[CrossRef](#)]
33. Rodrigues, L.L.; Solis-Chaves, J.S.; Vilcanqui, O.A.C.; Filho, A.J.S. Predictive incremental vector control for DFIG with weighted-dynamic objective constraint-handling method-PSO weighting matrices design. *IEEE Access* **2020**, *8*, 114112–114122. [[CrossRef](#)]
34. Rodrigues, L.L.; Potts, A.S.; Vilcanqui, O.A.C.; Filho, A.J.S. Tuning a model predictive controller for doubly fed induction generator employing a constrained genetic algorithm. *IET Electr. Power Appl.* **2019**, *13*, 812–819. [[CrossRef](#)]
35. Rodrigues, L.L.; Velasquez, O.C.; Lourenço, L.F.N.; Vilcanqui, O.A.C.; Salles, M.B.C.; Filho, A.J.S. Filtered Repetitive MPC applied to DFIG Grid Side Converter frequency support in microgrids during island operation. *IEEE Access* **2023**, *11*, 80835–80853. [[CrossRef](#)]
36. Shahidi, N.; Salary, E. Enhancing grid-connected photovoltaic systems' power quality through a dynamic voltage restorer equipped with an innovative sliding mode and PR control system. *E-Prime-Adv. Electr. Eng. Electron. Energy* **2025**, *11*, 100875. [[CrossRef](#)]
37. Abdelaal, A.K.; Shaheen, A.M.; El-Fergany, A.A.; Alqahtani, M.H. Sliding mode control based dynamic voltage restorer for voltage sag compensation. *Results Eng.* **2024**, *24*, 102936. [[CrossRef](#)]

Disclaimer/Publisher's Note: The statements, opinions and data contained in all publications are solely those of the individual author(s) and contributor(s) and not of MDPI and/or the editor(s). MDPI and/or the editor(s) disclaim responsibility for any injury to people or property resulting from any ideas, methods, instructions or products referred to in the content.